Computers and Electrical Engineering 122 (2025) 109994

Contents lists available at ScienceDirect

Computers and Electrical Engineering

journal homepage: www.elsevier.com/locate/compeleceng

A quantum direct torque control method for permanent magnet synchronous machines

Dermouche Reda [a], Abderrahmane Talaoubrid [b], Mehdi Fazilat [c], Nadjet Zioui [c,*], Mohamed Tadjine [d]

[a] ENSTA, Faculté de Médecine - Ctre biomédicale, Bordj El Kiffan, Alger, Algérie
[b] USTHB, Bab Ezzouar, Alger 16111, Algérie
[c] Université du Québec à Trois-Rivières, 3351 Bd des Forges, Trois-Rivières, QC G8Z 4M3, Canada
[d] École Nationale Polytechnique, 10 Rue des Frères OUDEK, El Harrach, Algiers 16200, Algeria

ARTICLE INFO

Keywords:
Quantum Computing
Quantum Direct Torque Control (QDTC)
Quantum subtractor
Quantum AND gate
Quantum OR gate

ABSTRACT

This study compares classical direct torque control (DTC) methods with a proposed quantum direct torque control (QDTC) strategy for synchronous machines. A quantum comparator is developed by implementing a quantum subtractor between real numbers ranging from -100 % to +100 %, and a quantum sign function is developed using this digital quantum subtractor. The QDTC implementation involved the use of quantum versions of the classic logical AND and OR gates. Simulation results indicate that the QDTC method significantly reduces torque ripple, with a ripple torque factor of 0.0392 compared to 0.0417 for the classical DTC. The QDTC approach also required 5.2 % fewer commutations (9.81×10^4) compared to the classical approach (1.035×10^5), which increases the longevity of the power components. Finally, the total harmonic distortion (THD) was lower for the QDTC method compared to the classical strategy. The results indicate that the proposed QDTC method either matches or surpasses the performance of the classical method across several metrics. Specifically, the reduced torque ripple and commutation frequency leads to smoother motor operation and longer component lifespans, while lower THD is indicative of greater motor efficiency.

1. Introduction

Permanent magnet synchronous motors (PMSMs) possess several notable advantages, including a high-power density, stable output torque, robust starting torque, long lifespan, high power factor, low noise, and good speed regulation performance [1], which can reduce the impact of torque fluctuations on the motor bearings and increase the service life of the entire machine system [2]. Consequently, PMSMs are the first choice in many applications, including complex systems like electric vehicles, flight control applications [3], precision machine tools, and industrial robots [4], as well as household tools such as home electric appliances, air conditioners, building ventilation, pumps, and fans [2]. Due to their widespread across multiple fields [1], research into energy-saving control technology for PMSMs holds significant commercial and societal value. In particular, PMSMs are projected to play a critical role in the near future as the demand for electric vehicles grows. PMSMs are 15 % more efficient than induction motors (IM) due to their high power density. Indeed, it is expected that more than 80 % of all electric vehicles will employ PMSMs in the near future [5].

* Corresponding author.
E-mail address: nadjet.zioui@uqtr.ca (N. Zioui).

https://doi.org/10.1016/j.compeleceng.2024.109994
Received 20 August 2024; Received in revised form 26 November 2024; Accepted 6 December 2024
Available online 14 December 2024

Nomenclature

Notations

R_s	The stator resistance (in Ω).
i_d	The *d* component of the current in the d-q frame (in A).
i_q	The *q* component of the current in the d-q frame (in A).
φ_d	The *d* component stator flux in a two-phase rotating d-q coordinate system (in Wb).
φ_q	The *q* component stator flux in a two-phase rotating d-q coordinate system (in Wb).
φ_f	The flux linkage due to the rotor magnets linking the stator (in Wb).
ω_e	The electrical angular speed of the rotor (in rad/s).
J	The inertia constant (in $kg.m^2$).
T_{em}	The electromechanical torque (in N.m).
T_r	The resistive torque (in N.m).
f	The friction coefficient (in N.m.s/rad).
Ω	The angular velocity of the motor (in rad/s).
p	The number of pole pairs of the machine (dimensionless).
S_A, S_B, S_C	The a, b, and c switches in the converter arms.
S_1, …,S_6	The six switches of the converter.
U_{AB}, U_{BC}, U_{CA}	The compound voltages at the output of the three-phase inverter (in V).
U_{AN}, U_{BN}, U_{CN}	The voltages with reference to the neutral point (in V).
U_{DC}	The DC voltage (in V).
φ_s	The stator flux (in Wb).
V_s	The stator voltage vector (in V).
I_s	The stator current (in A).
φ_{s0}	The stator flux at the initial stator flux (in Wb).
L_s	The stator inductance (in H).
θ_e	The electrical rotor angle (in rad).
δ	The load angle between $\varphi_s$and φ_r (in rad).
ν_1, … ν_6	The sectors vectors.
N	The zone number.
$I_{s\alpha}$	The α component of the current in the α, β frame.
$I_{s\beta}$	The β component of the current in the α, β frame.
C_{flx}	The Boolean flux controller output.
$\Delta\varphi$	The hysteresis limitations of the flux (in Wb).
ζ_{Tem}	The difference between the reference torque and its estimated value (in N.m).
h_T	The hysteresis bandwidth of the torque corrector (in N.m).
C_T	The Boolean torque controller output.
$\|q\rangle$	The qubit state.
$\|0\rangle$ and $\|1\rangle$	The two quantum eigenstates.
R_y	The y-axis quantum rotation gate.
$\|q_1q_2\rangle$	Tensor product between the qubit states $\|q_1\rangle$ and $\|q_2\rangle$.
$S\theta$	The cosine of the angle θ.
$S\theta$	The sine of the angle θ.

Abbreviations

CNOT	Controlled NOT gate.
CCNOT	Controlled CNOT gate.
DC	Direct current.
CHB	Cascaded H-bridge.
DFOC	Direct field oriented control.
d-q	Direct-quadrature,
DSIM	Double star induction machine
DTC	Direct torque control.
FC	Flying capacitor.
FOC	Field oriented control.
GTOs	Gate turn-off thyristors.
HHL	Harrow–Hassidim–Lloyd algorithm.
IGBTs	Insulated Gate Bipolar Transistors.
IMs	Induction Machines.
MOSFET	Metal-Oxide-Semiconductor Field-Effect Transistor.

NPC	Neutral Point Clamp.
PI	Proportional Integral.
PMSM	Permanent Magnet Synchronous Motor.
PWM	Pulse Width Modulation.
VV	Voltage Vector.
QDTC	Quantum Direct Torque Control.
SVM	Space Vector Modulation.
THD	Total Harmonic Distortion.

Vector control operation is preferred for motor drives due to its superior dynamic response. The most common vector control methods include the field-oriented control (FOC) and direct torque control (DTC) methods, which are still widely used in the present day [6].

The FOC method, proposed by Blaschke in 1971, is a rotor-field-oriented vector control method characterised by the independent control of flux and torque by separating the stator currents of a three-phase induction motor into the flux and current components of the motor. In contrast, the DTC method, proposed by Takahashi in 1986 [7], is a stator-field-oriented vector control method characterised by the independent control of the actual flux and torque of the motor within the hysteresis band around the specified reference flux and momentum. Both methods aim to control the torque and flux of the motor independently while being relatively insensitive to parameter changes.

The traditional DTC method in PMSMs was proposed by Shriwastava et al. [8] and Zheng et al. [9] at the Nanjing University of Aeronautics and Astronautics of China. DTC systems are generally superior to FOC methods due to their reduced dependence on machine parameters and excellent dynamic torque response [10]. Perhaps most importantly, the position signal and the current controllers used in vector control methods are not necessary for PMSM DTC drives. Instead, the voltage vector can be directly controlled using a pre-design look-up table, and torque and flux control is based on the hysteresis comparators [9].

DTC is the dominant control strategy in highly dynamic applications [11]. El Ouanjli et al. [12] conducted a comparative study between FOC and DTC strategies and demonstrated that DTC outperforms FOC in terms of torque and flux DSIM dynamics, as well as implementation complexity. Similarly, Sadouni and Meroufel [13] compared the direct field-oriented control (DFOC) and DTC strategies for a double star induction machine (DSIM) and demonstrated that DTC outperformed DFOC in terms of dynamic flux control. DTC also provides faster torque dynamics and is less sensitive to machine parameters.

Given the exceptional qualities and high-performance attributes of DTC, there has been a significant amount of research into utilising this control technique in both PMSMs and induction machines (IMs). The major benefits of DTC-functioned motor drives are their simplicity, reliability, and how they offer direct control over flux and torque. During DTC operation, the final voltage vector is selected to minimise torque and flux ripples [14]. This is achieved by using the flux and torque error outputs of the hysteresis controllers as well as the position of the flux vector to construct a switching table.

Several methods have been developed to improve DTC performance. One such method is DTC-SVM, which allows for the independent control of flux and torque through two proportional integral (PI) controllers and generates the desired voltage using the space vector modulation (SVM) technique [15]. Another approach to enhancing DTC is the deadbeat DTC technique. Unlike DTC-SVM, deadbeat control replaces the PI controllers with an inverse machine model. This model is solved to determine the necessary inputs (direct-quadrature d-q voltage) required to achieve the desired outputs (torque and stator flux) within a single pulse width modulation (PWM) period. Another method of enhancing DTC performance is the use of multilevel inverters rather than the standard two-level inverter. This scheme allows for a greater number of active voltage vectors that can be used to minimise the torque ripples [16]. There are several types of multilevel inverters used in DTC systems, including the three-level neutral point clamp (NPC), flying capacitor (FC), cascaded H-bridge (CHB), and the dual inverter technique using open-end winding configurations [17].

Other attempts to improve the DTC strategy have been investigated, such as by combining the DTC with predictive control, where the optimised switching state is selected to significantly minimize torque ripples [18]. To design a stable control function for the adaptive control of stator resistance and load torque [19], the backstepping control is commonly applied to the DTC of PMSM systems; this is occasionally combined with the adaptive control algorithm in some contributions [13]. Further improvements in motor torque response can be achieved by using intelligent techniques such as genetic algorithms, fuzzy logic, artificial neural networks, and neuro-fuzzy control algorithms [20].

Quantum computing is a new paradigm that offers exceptionally high computational performance compared to classic computers. This technology has been successfully utilised in many engineering modelling and control applications [21]. Indeed, quantum computing often outperforms classic control strategies in terms of computing time and resource efficiency [22–24]. For example, Zioui et al. [25] proposed a quantum version of the sliding mode controller using qubit states, with one qubit state used to encode the tracking error and another qubit state used to encode the time derivative of the error. The authors proposed a quantum circuit that proved to be as efficient as the classic counterpart with less energy consumption and less disruption of the control signal and validated their results using simulations with a DC motor as a test application. Quantum state domain equation and feedback control have also been addressed by using either the Harrow–Hassidim–Lloyd (HHL) algorithm [26] or quantum spins to express the state derivatives, while a hybrid quantum linearising-backstepping controller has also been implemented [27,28].

Saidat et al. [29] proposed a novel quantum version of the pulse-width modulation (PWM) algorithm implemented in a DC motor drive. A breakthrough contribution, the authors proposed that a quantum comparator between two real numbers ranging from 0 to 100 % could be used in a wide range of engineering applications.

This study proposes the concept of a quantum direct torque control (QDTC). To the best of our knowledge, this is the first time that a quantum formulation of the DTC has been proposed. This work presents multiple contributions to the field, including the proposal of an improved version of the real number comparator that considers values ranging from −100 % and +100 %. Based on the logical — i.e., Boolean — formulation of the DTC algorithm, the proposed quantum formulation uses quantum gates to translate the classic DTC into its quantum formulation. The investigation introduces a QDTC framework designed to enhance the control methodologies of PMSMs and includes several key advancements.

First, we have developed and integrated a quantum comparator and a sign function within the QDTC scheme. This quantum-driven approach enhances overall control mechanisms and leads to a reduction in switching frequency and torque order compared to classic DTC techniques. Second, our research proposes a quantum version of classical logic gates — specifically the AND and OR gates — utilising quantum circuits such as Toffoli and controlled NOT (CNOT) gates to create an efficient quantum formulation of the DTC algorithm. Third, our QDTC methodology improves several critical performance metrics, including minimised torque demand, reduced switching frequency, and lower total harmonic distortion, all of which contribute to improved motor efficiency, smoother operation, and the extended lifetime of power components. These findings are supported by comprehensive MATLAB Simulink simulations, demonstrating the superior performance of QDTC in comparison to classical DTC in dynamic motor control scenarios.

Our research represents an endeavour to apply quantum computing principles to motor control systems, laying the foundation for future research into hybrid classical-quantum control methodologies and contributing to the evolution of quantum computing applications in electrical engineering. Finally, this study compares both classic and quantum control strategies in PMSM applications.

The rest of the manuscript is structured as follows. Section 2 describes the tools and methods used in this study, including the techniques used to model the PMSM, the inverter, and DTC mechanisms. A detailed derivation of the quantum comparator and its implementation in the proposed QTDC strategy is also presented in this section. Section 3 elaborates on the proposed method for translating the classical DTC into its quantum counterpart, including the quantum logic-based control scheme. Section 4 presents and discusses the results of the simulations and compares the QDTC performance against the classical DTC approach across key metrics such as torque ripple, switching frequency, and total harmonic distortion. Section 5 concludes the study by summarising key findings, discussing the advantages of the quantum-based approach, and suggesting directions for future research, particularly regarding experimental validation and potential enhancements in quantum control procedures.

2. Tools and methods

2.1. PMSM and inverter modelling

2.1.1. The PMSM model

The PMSM model, in the synchronous d-q reference frame (see Fig. 1), and without consideration of core material saturation, eddy current, and hysteresis losses, is given by the electrical Eqs. 1 and 2 [5]:

$$\begin{cases} u_d = R_s i_d + \dfrac{d\varphi_d}{dt} - \omega_e \varphi_q \\ u_q = R_s i_q + \dfrac{d\varphi_q}{dt} + \omega_e \varphi_d \end{cases} \tag{1}$$

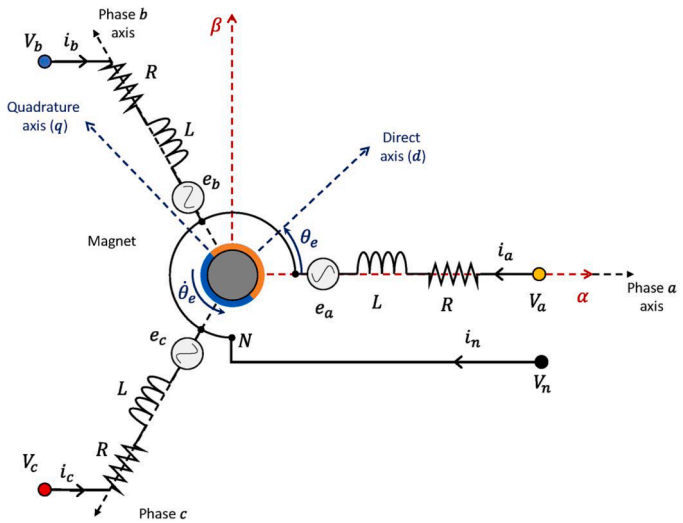

Fig. 1. The equivalent schematics of a PMSM.

$$\begin{cases} \varphi_d = L_d i_d + \varphi_f \\ \varphi_q = L_q i_q \end{cases} \tag{2}$$

R_s stator resistance (Ω),
i_d, i_q the components of the current (A),
φ_d and φ_q the d and q component stator flux in a two-phase rotating d-q coordinate system (Wb), respectively,
φ_f flux linkage due to the rotor magnets linking the stator (Wb),
ω_e the electrical angular speed of the rotor (rad/s).
Mechanical Eqs. 3 and 4 [30], which are obtained by applying the second law of Newton for rotations, are as follows:

$$J\frac{d\Omega}{dt} = T_{em} - T_r - f\Omega \tag{3}$$

$$T_{em} = \frac{3}{2}p\left(\varphi_f i_q + \left(L_d - L_q\right) i_d i_q\right) \tag{4}$$

J inertia constant (in kg.m^2),
T_{em} electromechanical torque (in N.m),
T_r resistive torque (in N.m),
f friction coefficient (in N.m.s/rad),
Ω angular velocity of the motor (in rad/s),
p number of pole pairs of the machine (dimensionless).

2.1.2. The inverter model

The voltage inverter is a static converter composed of commutation cells that are similar to transistors or Gate turn-off thyristors (GTOs) for high-power applications [13]. It enables the application of variable amplitude and frequency pulses to a machine system connected to a conventional grid. Following this adjustment, a filtered voltage U_{DC} is applied to the inverter, which serves as the synchronous machine's control centre and operates similarly to a power amplifier [17].

A three-phase inverter's control is managed by a switch arm. Each arm comprises two separate switches that correspond to the following Boolean states [5]:

$S_{A,B,\ C} = 1$: The switch of the highest half arm is closed.
$S_{A,B,\ C} = 0$: The switch of the highest half arm is opened.
Fig. 2 presents the schematics of a three-phase inverter feeding a synchronous machine.

For simplicity's sake, the switching of the switches' Boolean states is assumed to be instantaneous, the voltage drop across the switches is neglected, and the three-phase load is assumed to be balanced, star-coupled with isolated neutral.

The compound voltages at the output of the three-phase inverter of Fig. 2 are given by the following relationships [31]:

$$\begin{cases} U_{AB} = U_{AO} - U_{BO} \\ U_{BC} = U_{BO} - U_{CO} \\ U_{CA} = U_{CO} - U_{AO} \end{cases} \tag{5}$$

The three voltages U_{AO}, U_{BO}, and U_{CO} can be expressed with reference to the neutral point using the synchronous machine voltages

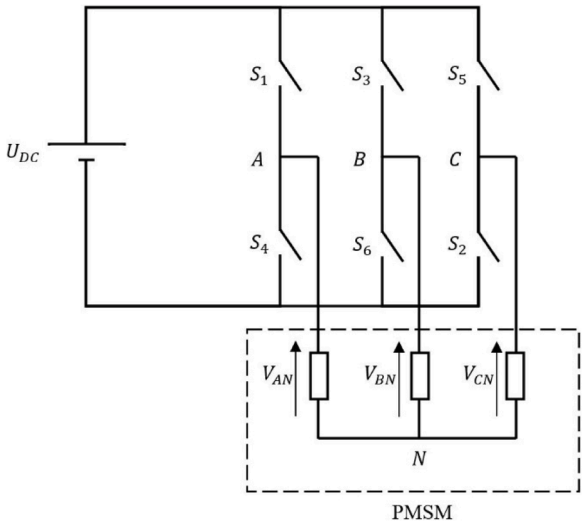

Fig. 2. Three-phase inverter with synchronous machine.

U_{AN}, U_{BN}, and U_{CN} as follows [31]:

$$\begin{cases} U_{AO} = U_{AN} + U_{NO} \\ U_{BO} = U_{BN} + U_{NO} \\ U_{CO} = U_{CN} + U_{NO} \end{cases} \tag{6}$$

With the assumption that the load is balanced with isolated neutral, the sum $U_{AN} + U_{BN} + U_{CN} = 0$ is valid. This implies that $U_{NO} = \frac{1}{3}(U_{AO} + U_{BO} + U_{CO})$, resulting in the following Eq. [31]:

$$\begin{cases} U_{AN} = \frac{2}{3}U_{AO} - \frac{1}{3}U_{BO} - \frac{1}{3}U_{CO} \\ U_{BN} = -\frac{1}{3}U_{AO} + \frac{2}{3}U_{BO} - \frac{1}{3}U_{CO} \\ U_{CO} = -\frac{1}{3}U_{AO} - \frac{1}{3}U_{BO} + \frac{2}{3}U_{CO} \end{cases} \tag{7}$$

Eq. 7 can also be expressed using the Boolean variables S_A, S_B, and S_C that represent the state of the switches (i.e., open or closed), similar to Eq. 4 [13].

$$\begin{cases} U_{AN} = \frac{U_{DC}}{3}(2S_A - S_B - S_C) \\ U_{BN} = \frac{U_{DC}}{3}(-S_A + 2S_B - S_C) \\ U_{CO} = \frac{U_{DC}}{3}(-S_A - S_B + 2S_C) \end{cases} \tag{8}$$

2.2. DTC control

DTC is determined by the instantaneous value of the voltage vector as well as the orientation of the stator flux. A three-phase inverter generates eight instantaneous base voltage vectors of which two are zero. These vectors are selected from a switching table depending on the flux and torque errors as well as the position of the stator flux vector. Unlike other techniques, DTC does not require the rotor position to select the voltage vector; instead, it requires a stator-linked reference frame. This characteristic makes DTC the best method for controlling alternating current machines without the usage of mechanical sensors [30,31]. Based on the measurement of the direct voltage at the inverter's input as well as the currents of the stator phases, the algorithm supplies the following variables at each time step:

- The stator flux in the motor.
- The actual electromagnetic torque.
- The sector number.

The torque and flux control strategy is based on the following procedure [7]:

- The temporal domain is separated into intervals of limited duration.
- At each instant, the line currents and voltages per phase of the PMSM are monitored.
- The components of the stator flux vector are calculated.
- The electromagnetic torque of the PMSM is determined by the estimated stator flux and the measured line current.
- The operating sequence of the inverter is determined to control the flux and torque according to a logic that is provided by the switching table [32].

To efficiently control torque in a synchronous machine, the flux must first be properly adjusted. In DTC control, it is the stator flux that is adjusted because it has a faster dynamic response than the rotor flux. This is because the rotor time constant is greater than that of the stator; consequently, variations in the rotor flux are negligible compared to that of the stator flux [32].

2.2.1. Behaviour of the stator flux and electromagnetic torque

Direct torque control is dependent on stator flux orientation. The expression of the stator flux in the reference frame linked to the stator of the machine is obtained by the following Eq. [8,13]:

$$\varphi s(t) = \int_0^t (Vs - R_s I)dt + \varphi_{s0} \tag{9}$$

φ_s stator flux (Wb),
V stator voltage vector (V),
I_s stator current (A),

φ_{s0} stator flux at the initial stator flux (Wb).

In cases where a non-zero voltage vector is applied during a time interval [0, T_e], the expression $V_s \gg R_s I_s$ holds true. In such cases, Eq. 4 can be rewritten as the following [33]:

$$\varphi_s(t) = \varphi_s(0) + V_s T_e \tag{10}$$

Eq. 10 leads to the derivation of Eq. 11, which implies that the end of the stator flux vector, $\varphi_s(t)$, moves on a straight line whose direction is given by the applied voltage vector V_s, as illustrated by Fig. 3 [8,33].

$$\Delta\varphi_s(t) = \varphi_s - \varphi_s(0) = V_s T_e \tag{11}$$

The flux (or radial) component affects the amplitude of φ_s, while the torque (or tangential) component affects its position.

By selecting an appropriate sequence of vectors V_s over control periods T_e, and assuming that the period T_e is very small compared to the rotation period of the stator flux, it is possible to operate with a practically constant flux module φ_s whose head follows a circular trajectory.

When the voltage vector V_s is non-zero, the time derivative $\frac{d\varphi_s}{dt}$ determines the direction and speed of the movement of φ_s.

If the term $R_s I_s$ is neglected, then $V_s = \frac{d\varphi_s}{dt}$. In this case, the rotation speed of φ_s depends significantly on the choice of V_s. It is maximised when vector V_s is perpendicular to the direction of φ_s and zero for a zero vector. It can also be negative.

Among the various forms used to describe synchronous machines, DTC techniques are usually implemented on models that use flux, stator current, and rotation speed as state variables. These models are typically presented in the stator reference frame (α, β) and are represented by the following system of Eqs. [5,7]:

$$\overline{v_s} = R_s \bar{I}_s + \frac{\mathrm{d}\overline{\varphi}_s}{\mathrm{d}t} \tag{12}$$

$$\begin{cases} \overline{\varphi}_s = L_s \bar{I}_s + \overline{\varphi_f} \\ \varphi_f = |\varphi_f| * e^{j\theta_e} \end{cases} \tag{13}$$

L_s stator inductance (in H),

φ_f rotor flux linkage (in Wb),

θ_e electrical rotor angle (in rad).

These Eqs. demonstrate that the vector $\overline{\varphi}_s$ can be controlled using the vector $\overline{v_s}$. In other words, the rotor follows the rotation of $\overline{\varphi}_s$.

The electromagnetic torque T_{em} can be expressed using Eq. 14. Its variation can be computed using Eq. 15 assuming that variations in stator flux amplitude are negligible [5,7].

$$T_{em} = \frac{3}{2}\frac{p}{L_s}\varphi_s\varphi_f \sin\delta \tag{14}$$

$$\Delta T_{em} = \left(\frac{p}{L_s}\varphi_s\varphi_f \cos\delta\right)\Delta\delta \tag{15}$$

δ load angle between $\varphi_s$and φ_f (in rad)

Eq. 15 shows that δ must increase to increase the torque. Since the rotation of the rotor flux depends on the rotor speed, the stator

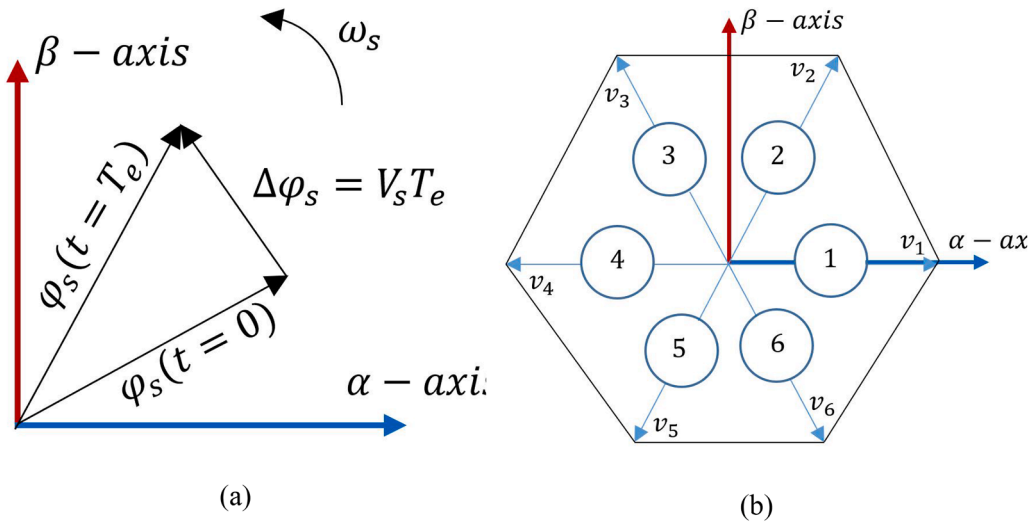

Fig. 3. (a) Evolution of the stator flux and (b) operating sequences.

flux must rotate faster than the rotor for δ to increase. We can thus say that the torque is controlled by the speed of rotation of the flux, which is, in turn, primarily controlled by the quadratic component of the voltage.

2.2.2. Estimation of stator flux and electromagnetic torque

Using the switches (S_A,S_B,S_C) to select the vector $\overline{v_s}$ allows for movement of the flux vector $\overline{\varphi_s}$ at a constant amplitude. The choice of $\overline{v_s}$ is dependent on the intended variation for the stator flux module $\overline{\varphi}$, the direction of rotation of $\overline{\varphi_s}$, and the desired development for the torque. To define the range of possible trajectories of $\overline{\varphi_s}$ in the reference frame (S), the latter can be decomposed into six zones calculated from components of the flux in the (α, β) plane as shown in Fig. 4 [31].

For example, when the flux $\overline{\varphi_s}$ is positioned in the first zone, the flux and torque can be controlled by selecting one of the following six voltage vectors [34]:

The selection of different voltage vectors results in different behaviours. Selecting v_2 leads to an increase in $\overline{\varphi_s}$ and T_{em}. If v_3 is chosen, $\overline{\varphi_s}$ decreases but T_{em} increases. Selecting v_5 leads to a drop in $\overline{\varphi_s}$ and T_{em}. If v_6 is chosen, $\overline{\varphi_s}$ grows but T_{em} drops. Finally, if v_0 and v_7 are selected, the rotation of the flux $\overline{\varphi_s}$ is stopped, resulting in a decrease in torque, while vector $\overline{\varphi_s}$ remains unchanged.

However, the effect of the voltage vectors $\overline{v_s}$ depends on the position of the flux vector within zone N. In zone $N = 1$, the vectors v_2 and v_5 are perpendicular to the flux vector $\overline{\varphi_s}$, meaning that although the change in torque is relatively rapid, the amplitude of the flux does not change significantly. In contrast, vectors v_6 and v_3 only contribute a very small torque component, but can cause substantial flux fluctuations. The voltage vector $\overline{v_s}$ at the inverter's output is calculated using the torque and stator flux deviations, as well as a torque estimator [34].

The estimation of the stator flux can be accomplished using measurements from the stator voltage and current vector. The stator flux can be expressed in Eq. 16 [6,10,11,15]:

$$\begin{cases} \varphi_{s\alpha} = \int_0^t (\overline{v_s} - R_s \bar{I}_{s\alpha}) \mathrm{d}t \\ \varphi_{s\beta} = \int_0^t (\overline{v_s} - R_s \bar{I}_{s\beta}) \mathrm{d}t \end{cases} \tag{16}$$

The stator flux vector is calculated from its (α, β) axis components as follows [9,17]:

$$\overline{\varphi_s} = \varphi_{s\alpha} + j.\varphi_{s\beta} \tag{17}$$

The Clarke transformation is used in conjunction with current measurements (i_{sa}, i_{sb}, i_{sc}) to calculate components $i_{s\alpha}$, $i_{s\beta}$ of the stator current vector based on the following Eqs. [35]:

$$I_s = I_{s\alpha} + j \cdot I_{s\beta} \tag{18}$$

$$\begin{cases} I_{s\alpha} = i_{sa} \\ I_{s\beta} = \frac{1}{\sqrt{3}}(2i_{sb} + i_{sa}) \end{cases} \tag{19}$$

Consequently, the components $v_{s\alpha}$, $v_{s\beta}$ can be obtained from the input voltage of the inverter U_0 and the control states (S_A, S_B,S_C) as

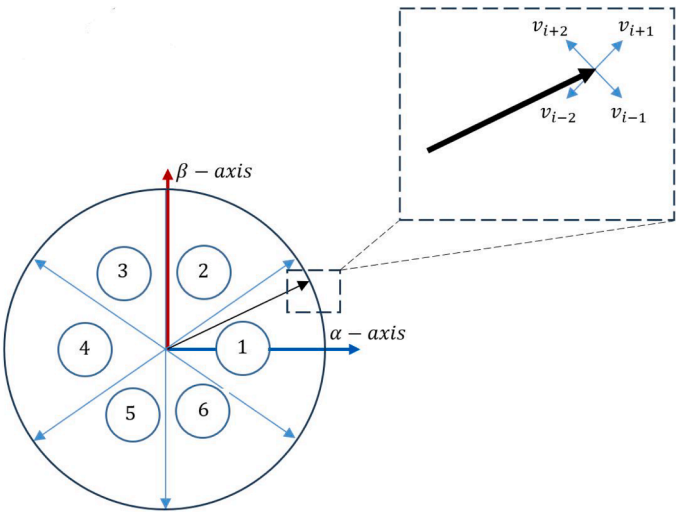

Fig. 4. Selection of the voltage vector V_s according to the operating zone.

follows [35]:

$$\begin{cases} v_{s\alpha} = \frac{1}{3}U_0\left(S_A - \frac{1}{2}(S_B - S_C)\right) \\ v_{s\beta} = \frac{\sqrt{3}}{3}U_0(S_B - S_C) \end{cases} \tag{20}$$

The module and the phase of the stator flux can be written as follows [6,10,13,15]:

$$|\varphi_s| = \sqrt{\varphi_{s\alpha}^2 + \varphi_{s\beta}^2} \tag{21}$$

$$\theta_s = \text{arctg}\frac{\varphi_{s\alpha}}{\varphi_{s\beta}} \tag{22}$$

Finally, the electromagnetic torque can be estimated from the estimated fluxes and measured currents using Eq. 23 [13,15]:

$$T_{em} = \frac{3}{2}p(\varphi_{s\alpha}i_{s\beta} - \varphi_{s\beta}i_{s\alpha}) \tag{23}$$

2.2.3. Flux and torque control strategies

The flux controller operates by trapping the flux vector in a circular ring as depicted in Fig. 5. The controller's output, represented by a Boolean variable C_{flx}, directly specifies whether the amplitude should be increased ($C_{flx} = 1$) or decreased ($C_{flx} = 0$) to maintain the desired difference between the flux and its reference φ_{sref} based on a specified limitation [32], as described in Eq. 24.

$$|\varphi_{sref} - \varphi_s| \leq \Delta\varphi \tag{24}$$

The controller law is such that [32]:

$$\begin{cases} Cflx = 1 \ if \ \Delta\varphi_s > \Delta\varphi \\ Cflx = 0 \ if \ \Delta\varphi_s \leq -\Delta\varphi \end{cases} \tag{25}$$

The stator flux error is defined as the difference between the flux reference value and the estimated value [7].

$$\varphi_{sref} - \varphi_s = \Delta\varphi_s \tag{26}$$

By introducing the difference $\Delta\varphi_s$ in a two-level hysteresis comparator (see Fig. 4), the value $C_{flx} = +1$ can be used to increase the flux, while the value $C_{flx} = 0$ is used reduce the flux). This also allows for exceptional dynamic performance.

To perform torque correction, the torque error ζ_{Tem} is defined as the difference between the reference torque T_{emref} and its estimated value T_{em}, as given in Eq. 27 [7,32]:

$$\zeta_{Tem} = T_{emref} - T_{em}. \tag{27}$$

The purpose of the torque correction is to ensure that the torque remains within the admissible limits defined in Eq. 28 [7,32]:

$$T_{emref} - T_{em} \leq h_T \tag{28}$$

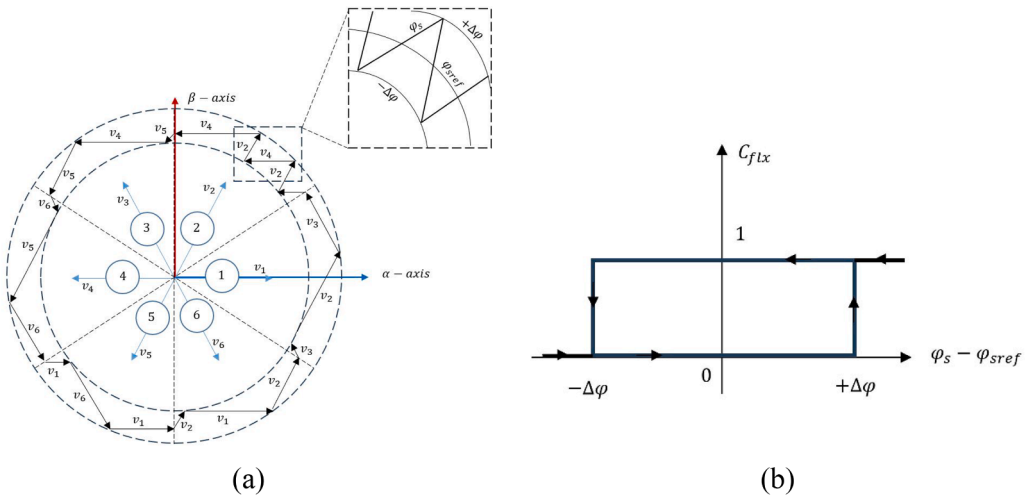

Fig. 5. (a) The selection of the corresponding voltage vectors and the (b) hysteresis flux controller.

h_T hysteresis bandwidth of the torque corrector.

Controllers can have two-level or three-level hysteresis designs. This study only considers two-level hysteresis controllers; these controllers are the same as the flux controller presented in Fig. 5b.

The control table is constructed based on the variables C_{flx}, C_T, and zone Z, which specify the position of the stator flux vector ϕ_s. Several switching tables can be employed to control the torque and stator flux [34]. Table 1 presents the control table for a two-level hysteresis torque and flux controllers.

The table includes only active (non-zero) voltage vectors, which serve to control stator flux and electromagnetic torque. These vectors either increase (C_{flx}= 1) or decrease (C_{flx} = 0) the flux depending on the flux position. At the same time, the forward active voltage vector increases torque (C_T= 1), while reverse vectors are used (C_T= 0) to decrease the torque when the output torque reaches the desired value. The use of only active voltage vectors to control torque allows for rapid changes in torque (higher torque slope) and increases switching frequency and torque ripple.

Fig. 6 illustrates the DTC technique for a synchronous machine. The performance of the DTC remains dependent on the careful selection of hysteresis bandwidths for the flux comparators and torque.

2.3. Basics of quantum computing

Unlike classic computing, quantum computing uses quantum bits, or qubits, to represent information. The qubit, or qubit state, $|q\rangle$ can be perceived as an infinite linear combination between the logic 0, denoted by $|0\rangle$, and the logic 1, denoted by $|1\rangle$. This can be expressed as follows:

$$|q\rangle = \alpha|0\rangle + \beta|1\rangle \tag{29}$$

In the above equation, α and β are complex numbers that represent the projections of $|q\rangle$ on the eigenstates $|0\rangle$ and $|1\rangle$, respectively. Eq. 29 can also be interpreted in terms of probabilities, such that $|\alpha|$ represents the probability that the state $|q\rangle$ is located at $|0\rangle$ and $|\beta|$ is the probability that the state $|q\rangle$ is located at $|1\rangle$.

In vector space, the eigenstates can be represented as two-dimensional vectors, where $|0\rangle \equiv \begin{pmatrix}1\\0\end{pmatrix}$ and $|1\rangle \equiv \begin{pmatrix}0\\1\end{pmatrix}$. Therefore, a given qubit state $|q\rangle$ can be expressed in the vector space as $\begin{pmatrix}\alpha\\\beta\end{pmatrix}$.

There are multiple quantum operators, called quantum gates, that can modify a qubit state; these can be represented as Hamiltonian matrices. The basic quantum operators that can be applied on a single qubit state are the Identity, X, Y, and Z gates, also known as the Pauli matrices σ_0, σ_x, σ_y, and σ_z, respectively; these are defined in Eqs. 30 to 33.

$$\sigma_0 = \begin{pmatrix}1 & 0\\0 & 1\end{pmatrix} \tag{30}$$

$$\sigma_x = \begin{pmatrix}0 & 1\\1 & 0\end{pmatrix} \tag{31}$$

$$\sigma_y = \begin{pmatrix}0 & -i\\i & 0\end{pmatrix} \tag{32}$$

$$\sigma_z = \begin{pmatrix}1 & 0\\0 & -1\end{pmatrix} \tag{33}$$

Other single qubit quantum gates can be expressed as a linear combination of the Pauli gates. These include the Hadamard gate (Eq. 34) as well as the three basic rotation gates (Eqs. 35–37).

$$H = \frac{\sqrt{2}}{2}\begin{pmatrix}1 & 1\\1 & 1\end{pmatrix} = \frac{\sqrt{2}}{2}(\sigma_0 + \sigma_x) \tag{34}$$

$$R_x(\theta) = \begin{pmatrix}cos\theta & -i\,sin\theta\\-i\,sin\theta & cos\theta\end{pmatrix} = cos\theta\ \sigma_0 - i\ sin\theta\ \sigma_x \tag{35}$$

Table 1
Control table for a two-level hysteresis torque controller.

Z		1	2	3	4	5	6
$C_{flx} = 1$	$C_T = 1$	v_2	v_3	v_4	v_5	v_6	v_1
	$C_T = 0$	v_6	v_1	v_2	v_3	v_4	v_5
$C_{flx} = 0$	$C_T = 1$	v_3	v_4	v_5	v_6	v_1	v_2
	$C_T = 0$	v_5	v_6	v_1	v_2	v_3	v_4

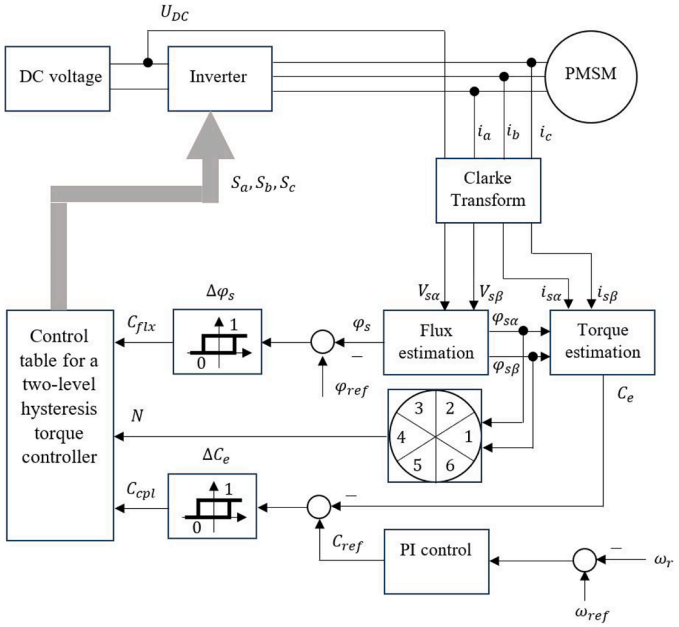

Fig. 6. Diagram of the general structure of a direct torque control (DTC) scheme.

$$R_y(\theta) = \begin{pmatrix} cos\theta & -sin\theta \\ sin\theta & cos\theta \end{pmatrix} = cos\theta\ \sigma_0 - i\ sin\theta\ \sigma_y \tag{36}$$

Table 2
The DTC logical table. X represents an undefined state.

	Torque	S_1	S_2	S_3	S_a	S_b	S_c
0	0	0	0	0	0	0	1
0	0	0	0	1	1	0	1
0	0	0	1	0	1	0	0
0	0	0	1	1	1	1	0
0	0	1	0	0	0	1	0
0	0	1	0	1	0	1	1
0	0	1	1	0	X	X	X
0	0	1	1	1	X	X	X
0	1	0	0	0	0	1	0
0	1	0	0	1	0	1	1
0	1	0	1	0	0	0	1
0	1	0	1	1	1	0	1
0	1	1	0	0	1	0	0
0	1	1	0	1	1	1	0
0	1	1	1	0	X	X	X
0	1	1	1	1	X	X	X
1	0	0	0	0	1	0	1
1	0	0	0	1	1	0	0
1	0	0	1	0	1	1	0
1	0	0	1	1	0	1	0
1	0	1	0	0	0	1	1
1	0	1	0	1	0	0	1
1	0	1	1	0	X	X	X
1	0	1	1	1	X	X	X
1	1	0	0	0	1	1	0
1	1	0	0	1	0	1	0
1	1	0	1	0	0	1	1
1	1	0	1	1	0	0	1
1	1	1	0	0	1	0	1
1	1	1	0	1	1	0	0
1	1	1	1	0	X	X	X
1	1	1	1	1	X	X	X

$$R_z(\theta) = \begin{pmatrix} e^{-i\theta} & 0 \\ 0 & e^{i\theta} \end{pmatrix} = cos\theta\ \sigma_0 - i\ sin\theta\ \sigma_z \tag{37}$$

3. Proposed method

3.1. Converting the DTC controller to a classic logic-based scheme

Table 2 represents the conversion of the DTC switching table to a logical table where the inputs are the flux controller output C_{flx}, the torque controller output, and the sector number in binary form (S_1,S_2, S_3), while the outputs are the switching state of the inverter (S_a, S_b, S_c) and the X state is the undefined state.

Logical Eq. 38 is derived from Table 2.

$$\begin{cases} S_a = \overline{C_{flx}}\ .\ S_2.S_3 + C_T.S_1 + \overline{C_T}.\overline{S_1}.\overline{S_2}.S_3 + \overline{C_T}.S_2.\overline{S_3} + C_{flx}\overline{S_1}.\overline{S_2}.\overline{S_3} \\ S_b = \overline{C_T}.S_2.S_3 + C_T.\overline{S_1}.\overline{S_2} + \overline{C_T}\ .\ S_1.\overline{S_3} + \overline{C_{flx}}\ .S_1.S_3 + C_{flx}.S_2.\overline{S_3} \\ S_c = C_T.S_2 + C_{flx}S_1.\overline{S_3} + \overline{C_T}.\overline{S_1}.\overline{S_2}.\overline{S_3} + \overline{C_T}\ .\ \overline{S_1}.\overline{S_2}.S_3 + \overline{C_{cpl}}\ .\ S_1.S_3 \end{cases} \tag{38}$$

3.2. Developing the quantum comparator

The proposed quantum comparator is based on the combination of a subtractor between two real numbers and a quantum sign detector function.

3.2.1. The quantum subtractor

The quantum subtractor between two real numbers is based on the tensor product between two real qubit states $|q_1\rangle = C\theta_1|0\rangle + S\theta_1|1\rangle$ and $|q_2\rangle = C\theta_2|0\rangle + S\theta_2|1\rangle$.

The two qubit states $|q_1\rangle$ and $|q_2\rangle$ are obtained following the application of a quantum rotation around the y-axis as follows:

$$|q_1\rangle = R_y(\theta_1)|0\rangle \tag{39}$$

$$|q_2\rangle = R_y(\theta_2)|0\rangle \tag{40}$$

The tensor product between $|q_1\rangle$ and $|q_2\rangle$ describes the four coefficients of the eigenstates as follows:

$$|q_1q_2\rangle = C\theta_1C\theta_2|00\rangle + C\theta_1S\theta_2|01\rangle + S\theta_1C\theta_2|10\rangle + S\theta_1S\theta_2|11\rangle \tag{41}$$

The coefficient of $|10\rangle$, which can be obtained by measuring the $|q_1q_2\rangle$ system at $|10\rangle$, can be rewritten using the following trigonometric property:

$$S\theta_1C\theta_2 = S\left(\frac{\alpha-\beta}{2}\right)C\left(\frac{\alpha+\beta}{2}\right) = \frac{1}{2}(S\alpha - S\beta) \tag{42}$$

where $\frac{\alpha-\beta}{2} = \theta_1$ and $\frac{\alpha+\beta}{2} = \theta_2$ and $\alpha = \theta_1 + \theta_2$ and $\beta = \theta_2 - \theta_1$.

Therefore, the computation of the subtraction between two real numbers x and y, such as $x = S\alpha$ and $y = S\beta$, can be achieved through the following steps:

Step 1. Compute $\alpha = Asin(x)$ and $\beta = Asin(y)$.
Step 2. Compute θ_1 as $\frac{\alpha-\beta}{2}$ and θ_2 as $\frac{\alpha+\beta}{2}$.
Step 3. Initialise $|q_1\rangle$ to $|0\rangle$ and $|q_2\rangle$ to $|0\rangle$.
Step 4. Perform quantum rotations $R_y(\theta_1)$ on $|q_1\rangle$ and $R_y(\theta_2)$ on $|q_2\rangle$.
Step 5. Measure the system at the state $|10\rangle$.

Only the computation of the coefficient should be performed on the state vector. This will provide half the subtraction result, which would normally be multiplied by 2 through the introduction of a gain. However, the subtraction only needs to identify the sign of the result to build a comparator. Therefore, there is no need to add a gain of 2, since the sign of a number is the same as the sign of its half.

Table 3
Truth table of the subtraction between two Boolean numbers.

a	b	$s = a - b$	r (borrow)
0	0	0	0
0	1	1	1
1	0	1	0
1	1	0	0

3.2.2. The quantum sign detector

The quantum sign detector is based on the concept of the borrow in Boolean subtraction, which is described in the truth table shown in Table 3.

According to Table 3, the only state where $r = 1$ is when $a = 0$ and $b = 1$. The logical expression of the borrow is $r = \overline{a}\ b$. When the borrow is 1, this implies that the subtraction is negative because a is less than b.

The quantum version of the logical expression of r can be performed using the quantum equivalent of the classic NOT gate, which is the X gate, as well as the quantum equivalent of the classic AND gate, which is the CCNOT (or Toffoli) gate. Fig. 7 presents the design of the quantum sign detector circuit.

3.3. Proposed quantum DTC

The quantum implementation of DTC uses the equivalent quantum circuits for the classic logic AND and logic OR based on the Boolean logic for DTC schematics (see Eq. 38). As previously mentioned, the classic AND gate can be implemented using a Toffoli gate, while the classic OR gate can be implemented using three qubit states. The first two qubit states as serve as two inputs, while the third qubit is initialised to $|0\rangle$ for computation purposes. The OR gate can be implemented using a CNOT gate between the first and third qubit states, followed by another CNOT gate between the second and third qubit states, before ending with a Toffoli gate. Fig. 8 depicts the quantum implementation of the classic AND and OR logical gates.

4. Results and discussion

4.1. Simulation setup and results

The simulation was carried out using MATLAB Simulink R2023b. Fig. 9 illustrates the overall framework of the simulation program, while Table 4 presents the parameters used.

The simulations were carried out at a nominal speed of 450 rad/s and a load of 2.8 Nm as the nominal torque applied at $t = 0.05$ s.

Figs. 10 and 11 present the simulated speed and torque using classic and quantum DTC approaches, respectively.

Figs. 12 and 13 present the simulated speed and torque errors for the classic and quantum DTC, respectively.

An additional analysis was performed for the total harmonic distortion (THD). The simulation results for both the current and THD of the classic and quantum SVPWM systems are presented in Figs. 14 and 15, respectively.

4.2. Discussion

Fig. 10 compares the simulated speed of a motor controlled using classic and quantum direct torque control. An analysis of the simulation results reveals that both control methods exhibited a rapid acceleration phase, reaching the target speed of 450 rad/s within approximately 0.03 seconds. The immediate response has a highly dynamic arrangement that is typically associated with DTC methods. Specifically, the reference speed is represented by a solid red line, while the speed responses of the classic and quantum methods are shown using dashed and dotted lines, respectively. Upon reaching this nominal speed, both the classic and quantum DTC methods maintain a speed of around 450 rad/s. The close alignment of the speed curves with the reference line for both control methods highlights the accuracy and effectiveness of both DTC strategies in supporting the desired speed under nominal load conditions. Following the application of the nominal load at 0.05 s, the system's response was well-damped. The stability observed in the speed response suggests that both control methods are capable of robust performances in terms of achieving and sustaining the target speed with minimal overshoot and steady-state error. The simulation results indicate that both the classic and quantum DTC methods can effectively control the motor speed, achieving near-instantaneous acceleration and stable operations at the target speed.

Upon analysing the torque response shown in Fig. 11, both control methods exhibit an initial torque output of around 3 Nm, closely matching the reference torque represented by the solid red line. During the steady-state operation, the torque response for both classic and quantum DTC (depicted by dashed and dotted lines), is closely aligned with the reference torque. A notable transient phenomenon appears at around 0.03 seconds, where the torque drops sharply to nearly 0 Nm. This transient reaction is due to the speed reaching its target value. However, both the classic and quantum DTC strategies handle this rapid transition effectively, demonstrating a sharp drop and subsequent stabilisation around the 0 Nm mark.

When the nominal load is applied at 0.05 s, the torque of both classical and quantum DTC rapidly follows the reference values. The

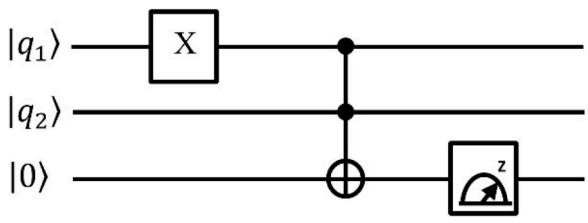

Fig. 7. The quantum sign detector circuit.

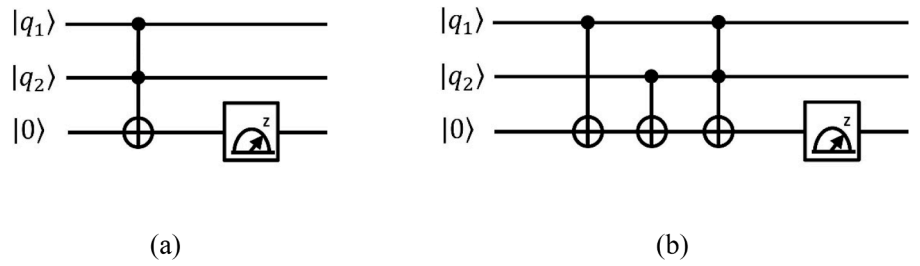

(a) (b)

Fig. 8. The quantum versions of the (a) classic AND gate and (b) classic OR gate.

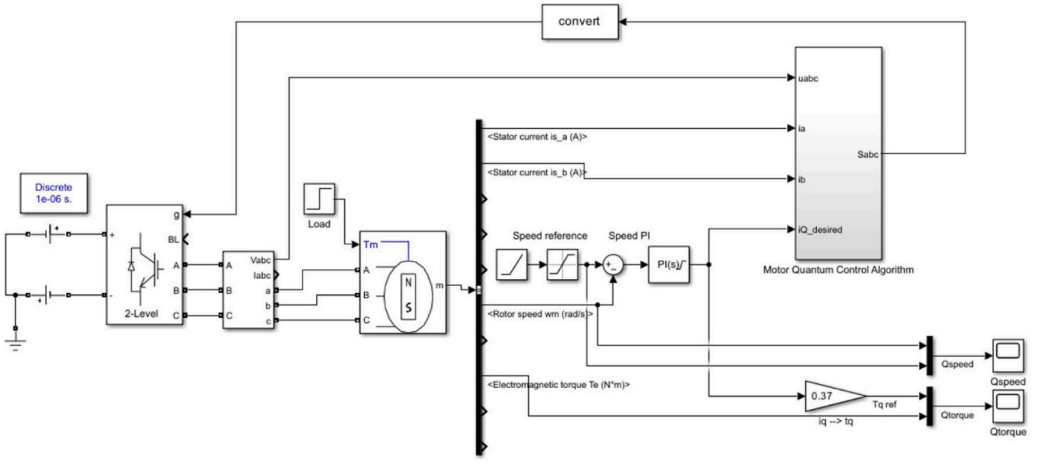

(a)

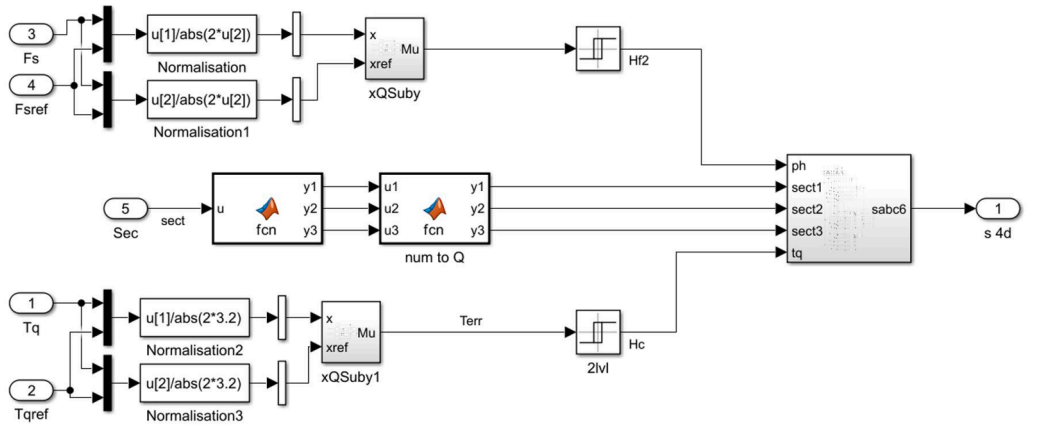

(b)

Fig. 9. Simulation program: (a) the whole Simulink program, (b) the pulse generation section of the program.

change in the load conditions highlights the responsiveness and stability of the control methods.

An important characteristic of torque control performance is the ripple observed in the torque signal. Both methods produce some degree of torque ripple around the nominal values. However, a detailed comparison reveals that the QDTC method exhibits slightly less ripple compared to its classic counterpart, with ripple torque factors of 0.0392 and 0.0417, respectively. Reduced torque ripple is advantageous to motor operations, as it results in smoother operation, reduced mechanical stress on the motor and drivetrain, and

Table 4
The parameters used for the simulation.

Parameter	Value (Unit)
Stator phase resistance R_s	1.6 (Ω):
Armature inductance L_s	0.006365 (H)
Flux linkage φ_f	0.1852 (Wb)
Inertia J	001854 (kg.m^2)
Viscous damping F	5.396e-6 (N.m.s)
Pole pairs p	2
Static friction T_f	0 (N.m)
Nominal Torque T_{emN}	2.8 (Nm)
Nominal voltage V_{DC}	300 (V)
Nominal Speed$N$	4250 (RPM)

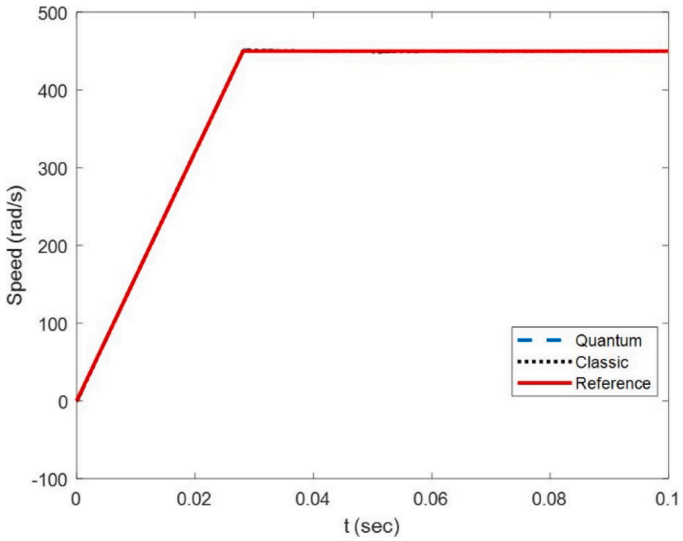

Fig. 10. Speed using classic and quantum DTC.

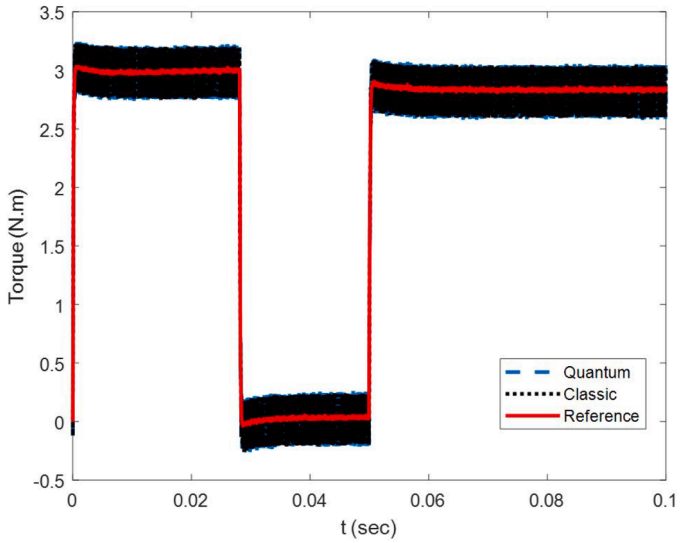

Fig. 11. Torque using classic and quantum DTC.

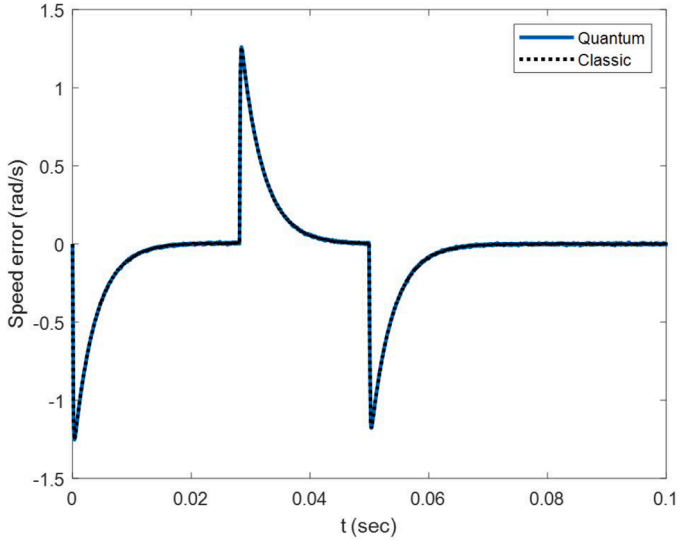

Fig. 12. Speed errors for classic and quantum DTC.

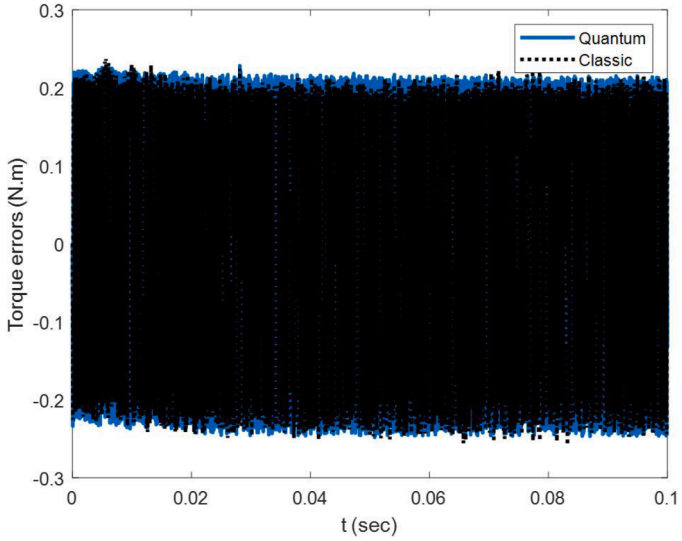

Fig. 13. Torque errors for classic and quantum DTC.

potentially lower acoustic noise. Overall, this analysis of the torque response emphasises the effectiveness of both DTC methods in achieving and maintaining the desired torque levels, even under rapid transient conditions. The QDTC method exhibits some potential advantages in terms of its reduced torque ripple, which can enhance the motor system's overall performance and longevity.

Fig. 12 compares the speed errors observed in the classic and quantum DTC strategies. The simulations were performed under the same conditions: a nominal speed of 450 rad/s and a nominal load torque of 2.8 Nm. Both control techniques exhibited similar accuracies in terms of speed regulation. Initially, there was a slight deviation in speed error as the motor accelerates towards the nominal speed, though this error was minimal for both methods, indicating a smooth initial acceleration phase. At approximately 0.03 seconds, the speed error peaks at approximately 1.3 rad/s for both control procedures, indicating a momentary overshoot in speed as the motor adjusts. This is a typical transient response as the control algorithms react to sudden changes in load or torque demand. Following this peak, the speed error quickly decreases and stabilises, demonstrating the effectiveness of both control approaches in correcting deviations in speed and maintaining accurate speed regulation. Another transient was observed at around 0.05 seconds when the speed error briefly decreased in response to the application of the torque load. Once again, the control algorithms responded rapidly, returning the speed error to near zero.

Overall, the steady-state speed error for both techniques remains close to zero, demonstrating a high accuracy of speed control. The close overlap of the error curves for both techniques indicates that they exhibit comparable performances in terms of speed regulation

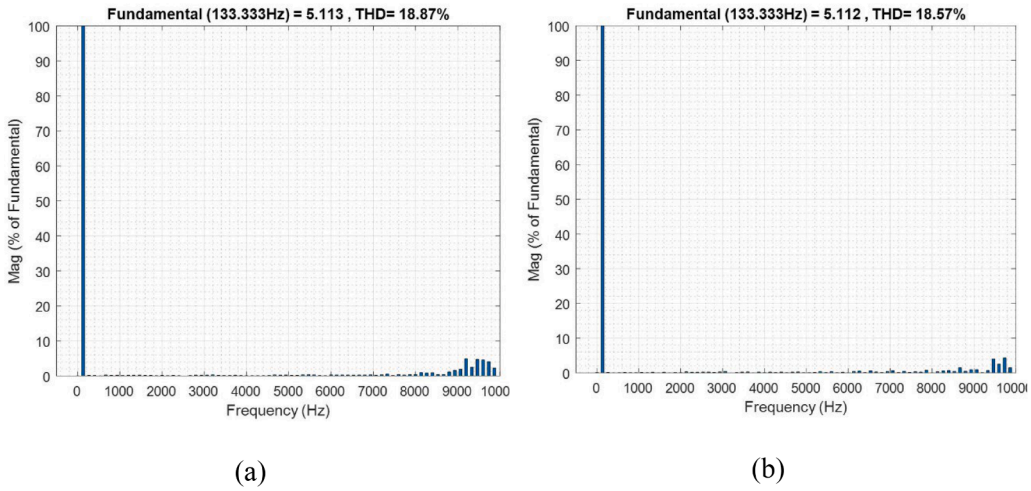

Fig. 14. Spectral analysis of the (a) classic DTC and (b) QDTC.

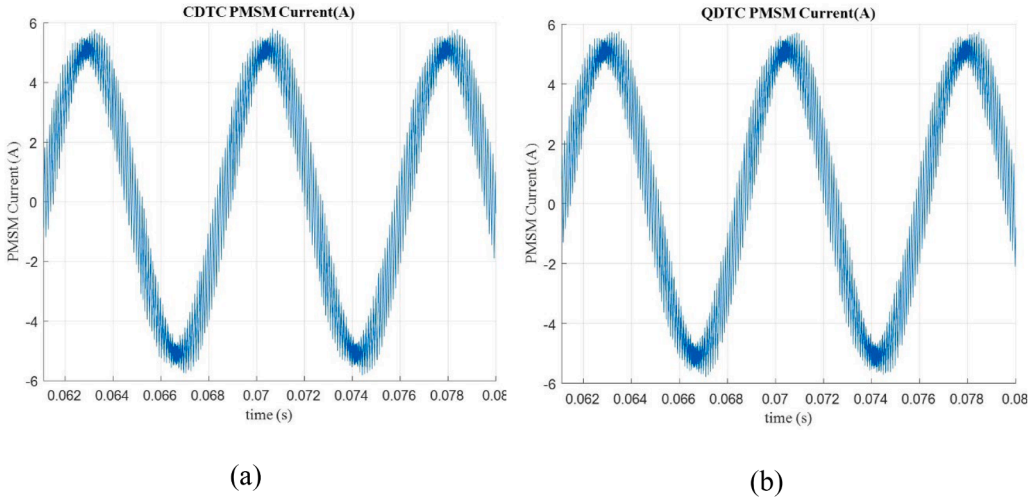

Fig. 15. Current wave for the (a) classic DTC and (b) QDTC.

under the specified simulation conditions. The analysis of speed error in this study highlights the robustness of DTC strategies in handling dynamic load conditions and maintaining precise speed control. The QDTC method did not exhibit any significant deviations in terms of speed error compared to the classic DTC method; this is particularly notable given the potential benefits of QDTC in other areas, such as its reduced torque ripple and fewer commutations.

Fig. 13 provides several crucial insights into the implementation of the two control processes. Torque error is a crucial measure as it indicates the deviation of the actual torque from the desired torque, which directly impacts the performance and efficiency of the motor. During the simulation, the torque error for both control methods remained within a narrow band that fluctuated around zero, indicating that both strategies preserved the desired torque with minimal deviation. Specifically, the error values oscillated within a range of approximately ± 0.2 Nm, which corresponds to the hysteresis band, highlighting the precision of the control schemes in terms of controlling torque. One notable observation was that the torque error exhibited high-frequency oscillatory behaviour; this is typical of DTC methods due to the hysteresis controllers. Both control procedures exhibited similar patterns in torque error oscillations, indicating that the QDTC method retains the fundamental characteristics of the classic DTC approach while providing benefits in other areas.

In general, the analysis conducted in this study reveals that both strategies positively minimised torque errors, ensuring that the motor drives were operating at close to the preferred torque value. Although high-frequency oscillations were present in both methods, these are tightly constrained within a narrow band, demonstrating robust performance in torque regulation.

The QDTC method performed slightly better with regard to the THD (Fig. 14). Specifically, the QDTC method exhibited a THD of 18.57 % compared to its classic counterpart, which had a THD of 18.87 %. It should be noted that both the quantum and classic DTC methods exhibit a fundamental frequency of 133.33 Hz and low-magnitude high harmonics (Fig. 5). This analysis shows that the QDTC

method exhibits significantly lower magnitudes for the harmonics. Due to the high-frequency harmonics in both classic and quantum DTC methods, the current waveform is relatively similar to a sine wave (Fig. 15).

The simulation results show that both classic and quantum DTC algorithms consume the same amount of energy for power switches. However, there was a clear difference in the number of commutations required for the two methods; specifically, the quantum DTC algorithm required 9.81×10^4 commutations, while the classic DTC algorithm required 1.035×10^5 commutations. The variance in the number of commutations has important implications for the performance and longevity of the power components used in motor control systems.

Commutations refer to the switching actions used by the inverter to alter the voltage vectors. Each commutation involves a switching event in the power transistors, which generates heat and causes wear over time. Motor control applications generally use standard power transistors, such as insulated gate bipolar transistors (IGBTs) or metal-oxide-semiconductor field-effect transistors (MOSFETs); these transistors are known to generate heat and wear over time.

This study employs a three-phase inverter with commutation cells, such as transistors or gate turn-off thyristors (GTOs), for high-power applications. These cells enable variable amplitude and frequency pulses to be applied to a machine over a conventional grid. A lower number of commutations is typically preferred in these systems as it leads to reduced mechanical and thermal stress on the switches, prolonging the lifespans of these components. A 5.2 % reduction in the number of commutations suggests that the QDTC technique can significantly improve the durability of power components and potentially increase the reliability of motor control applications. Fewer commutations translate to reduced switching losses, lower heat generation, and diminished mechanical fatigue, all of which contribute to prolonging the service life of the switches and lower maintenance costs. This highlights the potential benefits of the QDTC method with regard to the overall performance and sustainability of motor applications.

Overall, the QDTC approach has demonstrated significant potential in reducing torque surge, commutation frequency, and THD in motor control systems. However, it is necessary to recognise the limitations of this study. These findings are exclusively based on simulations, and there may be many challenges associated with the translation of quantum algorithms into physical hardware for real-world applications. Current quantum computing technology faces issues such as noise, qubit decoherence, and limited gate fidelity, which could impact the anticipated performance of QDTC in practical scenarios. Additionally, incorporating quantum algorithms into real-time motor control systems may introduce computational complexity and latency, especially for high-speed processing applications. Furthermore, the evaluation of QDTC in the study is limited to a specific case of PMSM control and does not consider its performance under diverse loads, speeds, and potential disruptions. Extending this approach to other motors or control systems should be the subject of future research. Finally, integrating quantum computing into existing control systems requires a hybrid classical-quantum approach, which is likely to encourage significant engineering and synchronisation challenges that must be addressed in future studies.

5. Conclusion

This study proposed and evaluated a QDTC method for synchronous machines, highlighting its advantages over classical DTC methods. The strategy leverages quantum computing principles to improve performance across a variety of metrics, including reductions in torque ripple and switching frequency, resulting in more efficient and durable motor control systems. Specifically, the QDTC method resulted in greatly reduced torque ripple, fewer commutations, and lower THD, outperforming its classical counterpart in these important areas. Our results suggest that the proposed QDTC process has the potential to create more economical, dependable, and long-lasting motor drives, particularly in applications that require accurate torque and speed control.

Future research should focus on the experimental validation of the QDTC technique under real-world conditions, optimising quantum algorithms for specific motor control tasks, and developing hybrid classical-quantum control strategies that leverage the strengths of both approaches. This includes expanding the scope of this study to other fields, such as control schemes for asynchronous machines, fault detection, optimisation, and predictive maintenance. In particular, the QDTC method must be validated on physical motor systems to assess its performance outside of theoretical simulations. Such validation experiments would help ascertain the efficacy of QDTC in addressing real-world challenges in quantum computing, such as noise, qubit decoherence, and thermal stability. Future research should also facilitate an evaluation of its effectiveness under diverse load conditions and operational scenarios.

Other examples of future research include attempts to reduce computational complexity and enhance real-time processing speeds by refining the quantum gate sequences and reducing qubit requirements. These studies would help mitigate concerns related to potential latency in high-speed applications. In addition, expanding the assessment of the proposed QDTC method beyond the specific PMSM case described in this study would also enhance its applicability. Finally, a potential field for investigation involves the development of hybrid classical-quantum control strategies. By incorporating the reliability and simplicity of classical DTC methods with the computational benefits of quantum techniques, these hybrid models could offer a more scalable and adaptable solution, especially in industrial applications where a complete transition to quantum computing may not be achievable.

CRediT authorship contribution statement

Dermouche Reda: Conceptualization, Methodology, Investigation, Data curation, Formal analysis, Writing – review & editing, Visualization. **Abderrahmane Talaoubrid:** Conceptualization, Methodology, Investigation, Data curation, Formal analysis, Writing – review & editing, Visualization. **Mehdi Fazilat:** Investigation, Formal analysis, Writing – review & editing, Visualization. **Nadjet Zioui:** Resources, Supervision, Project administration, Conceptualization, Methodology, Investigation, Data curation, Formal analysis, Writing – review & editing, Visualization. **Mohamed Tadjine:** Resources, Supervision, Project administration, Conceptualization,

Methodology, Investigation, Data curation, Formal analysis, Writing – review & editing, Visualization.

Declaration of competing interest

The authors declare that they have no known competing financial interests or personal relationships that could have appeared to influence the work reported in this paper.

Data availability

All data used to produce this work is included in the document.

References

[1] Sun W, Si H, Qiu J, Li J. Research on efficiency of permanent-magnet synchronous motor based on adaptive algorithm of fuzzy control. Sustainability 2024;16:1253. https://doi.org/10.3390/su16031253.

[2] Huang Q, Huang Q, Guo H, Cao J. Design and research of permanent magnet synchronous motor controller for electric vehicle. Energy Sci Eng 2023;11:112–26. https://doi.org/10.1002/ese3.1316.

[3] Karboua D, Toual B, Kouzou A, Douara BO, Mebkhouta T, Bendenidina AN. High-order supper-twisting based terminal sliding mode control applied on three phases permanent synchronous machine. Periodica Polytechnica Electr Eng Comput Sci 2023;67(1):40–50. https://doi.org/10.3311/PPee.21026.

[4] Rafael LD, Jaioneb GE, Cristinac L, Ibon SL. An Industry 4.0 maturity model for machine tool companies. Technol Forecast Soc Change 2020;159:120203. https://doi.org/10.1016/j.techfore.2020.120203.

[5] Meesala REK, Thippiripati VK. An improved direct torque control of three-level dual inverter fed open-ended winding induction motor drive based on modified look-up table. IEEE Trans. Power Electron. 2019;35(4):3906–17. https://doi.org/10.1109/TPEL.2019.2937684.

[6] Gundogdu A, Celikel R, Dandil B, Ata F. FPGA in-the-loop implementation of direct torque control for induction motor. Automatika 2021;62(2):275–83. https://doi.org/10.1080/00051144.2021.1934365.

[7] Alshbib MM, Alsofyani IM, Elgbaily MM. Enhancement and performance analysis for modified 12 sector-based direct torque control of ac motors: experimental validation. Electronics 2023;12:549. https://doi.org/10.3390/electronics12030549.

[8] Shriwastava RG, Wagh NB, Shinde SK. Implementation of DTC-controlled PMSM driven by a matrix converter. Int J Recent Technol Eng 2020;8(5):4420–4. https://doi.org/10.35940/ijrte.E6641.018520.

[9] Zheng X, Xue L, Wang P, Li J, Shen Z. Backstepping DTC control of PMSM with robust adaptive law. IOP Conf. Series: Materials Science and Engineering 2020;793:012033. https://doi.org/10.1088/1757-899X/793/1/012033.

[10] Dahmardeh H, Ghanbari M, Rakhtala SM. A novel combined DTC method and SFOC system for three-phase induction machine drives with PWM switching method. J Oper Automat Power Eng 2023;11(2):76–82. https://doi.org/10.22098/joape.2023.9717.1679.

[11] Meesala REK, Udumula RR, Nizami TK, Hosseinpour A. Development of enhanced direct torque control for surface-mounted permanent magnet synchronous motor drive operation. IET Power Electr 2022;16:1814–27. https://doi.org/10.1049/pel2.12504.

[12] El Ouanjli N, Derouich A, El Ghzizal A, Motahhir S, Chebabhi A, El Mourabit Y, Taoussi M. Modern improvement techniques of direct torque control for induction motor drives - a review. Protect Control Modern Power Syst 2019;4(11). https://doi.org/10.1186/s41601-019-0125-5.

[13] Sadouni R, Meroufel A. Performances comparative study of Field Oriented Control (FOC) and Direct Torque Control (DTC) of Dual Three Phase Induction Motor (DTPIM). Int J Circuits Syst Signal Process 2012;6(2):163–70.

[14] Eshwar K, Kumar TV. Reduction of torque and flux ripples in direct torque control for three-level open-end winding PMSM drive. IET Electr Power Appl 2021;14(14):2843–54. https://doi.org/10.1049/iet-epa.2020.0487.

[15] Laxmi Narasimha Rao Y, Ravindranath G. Implementation of DTC-SVM of induction motor using arduino UNO. In: 2nd International Conference on Applied Electromagnetics, Signal Processing, & Communication (AESPC). IEEE; 2021. https://doi.org/10.1109/AESPC52704.2021.9708524.

[16] Tarusan SAA, Jidin A, Jamil MLM. The optimization of torque ripple reduction by using DTC-multilevel inverter. ISA Trans 2022;121:365–79. https://doi.org/10.1016/j.isatra.2021.04.005.

[17] Salem M, Richelli A, Yahya K, Hamidi MN, Ang TZ, Alhamrouni I. A comprehensive review on multilevel inverters for grid-tied system applications. Energies 2022;15(17):6315. https://doi.org/10.3390/en15176315.

[18] Wang F, Li J, Li Z, Ke D, Du J, Garcia C, Rodriguez J. Design of model predictive control weighting factors for pmsm using gaussian distribution-based particle swarm optimization. IEEE Trans Indus Electr 2021;69(11). https://doi.org/10.1109/TIE.2021.3120441.

[19] Muduli UR, Chikondra B, Behera RK. Novel model predictive DTC for three-to-five phase direct matrix converter fed induction motor drive. In: 12th Energy Conversion Congress & Exposition - Asia (ECCE-Asia). IEEE; 2021. https://doi.org/10.1109/ECCE-Asia49820.2021.9479067.

[20] Gdaim S, Mtibaa A, Mimouni MF. Artificial neural network-based DTC of an induction machine with experimental implementation on FPGA. Eng Appl Artif Intell 2023;121:105972. https://doi.org/10.1016/j.engappai.2023.105972.

[21] Mahmoudi Y, Zioui N, Belbachir H, Tadjine M. A brief review on mathematical tools applicable to quantum computing for modelling and optimization problems in engineering. Emerg Sci J 2022;7(1):289–312. https://doi.org/10.28991/ESJ-2023-07-01-020.

[22] Zioui N, Mahmoudi A, Tadjine M. Representing quantum spins in different coordinate systems for modelling rigid body orientation. Karbala Int J Modern Sci 2023;9:460–72. https://doi.org/10.33640/2405-609X.3313.

[23] Fazilat M, Zioui N, St-Arnaud J. A novel quantum model of forward kinematics based on quaternion/Pauli gate equivalence: application to a six-jointed industrial robotic arm. Results Eng 2022;14(10):100402. https://doi.org/10.1016/j.rineng.2022.100402.

[24] Zioui N, Mahmoudi Y, Mahmoudi A, Tadjine M, Bentouba S. A new quantum-computing-based algorithm for robotic arms and rigid bodies' orientation. J Appl Comput Mech 2021;7(3):1836–46. https://doi.org/10.22055/JACM.2021.37611.3048.

[25] Zioui N, Mahmoudi A, Tadjine M. Developing and implementing a quantum algorithm for the sliding mode controller using multiple qubit operators: application to DC motor speed drive. Appl Sci Eng Prog 2024;17(2):7016. https://doi.org/10.14416/j.asep.2023.09.005.

[26] Boudjoghra MEA, Daimellah SAS, Zioui N, Mahmoudi Y, Tadjine M. State-Domain equationEqs. and their quantum computing solution based HHL algorithm. Math Modell Eng Probl 2022;9(4):879–86. https://doi.org/10.18280/mmep.090404.

[27] Zioui N, Mahmoudi Y, Mahmoudi A, Tadjine M. Quantum computing based state domain equationEqs. and feedback control. Results Appl Math 2023;19(1):100385. https://doi.org/10.1016/j.rinam.2023.100385.

[28] Zioui N, Mahmoudi A, Tadjine M. Design of a new hybrid linearising-backstepping controller using quantum state equationEqs. and quantum spins. Int J Autom Control 2023;17(4):397–417. https://doi.org/10.1504/IJAAC.2023.131754.

[29] Saidat S, Boumekhita R, Tadjine M, Zioui N. Quantum pulse-width modulation design and implementation for a DC motor drive. Quantum Inf Process 2024;23(88). https://doi.org/10.1007/s11128-024-04284-2.

[30] Mondal S, Roy P, Banerjee A, Mondal U. A CKF-based sensor-less FOC integrated with gh-SVPWM for PMSM drives. Electr Eng 2024;106:3461–73. https://doi.org/10.1007/s00202-023-02169-8.

[31] Medekhel L, Hettiri M, Labiod C, Srairi K, Benbouzid M. Enhancing the performance and efficiency of two-level voltage source inverters: a modified model predictive control approach for common-mode voltage suppression. Energies 2023;6:7305. https://doi.org/10.3390/en16217305.

[32] Allafi IM, Foster SN. Analysis of direct torque control response to stator and rotor faults in permanent magnet synchronous machines. Energies 2023;16:6940. https://doi.org/10.3390/en16196940.
[33] Elgbaily M, Anayi F, Alshbib MM. A combined control scheme of direct torque control and field-oriented control algorithms for three-phase induction motor: experimental validation. Mathematics 2022;10:3842. https://doi.org/10.3390/math10203842.
[34] Aziz AGMA, Abdelaziz AY, Ali ZM, et al. A comprehensive examination of vector-controlled induction motor drive techniques. Energies 2023;16(6):2854. https://doi.org/10.3390/en16062854.
[35] Kasri A, Ouari K, Belkhier Y, Bajaj M, Zaitsev I. Optimizing electric vehicle powertrains peak performance with robust predictive direct torque control of induction motors: a practical approach and experimental validation. Sci Rep 2024;14:14977. https://doi.org/10.1038/s41598-024-65988-0.